

Chapter 7

Water jet trajectory theory¹

7.1 Introduction

Predicting the trajectory and surface water distribution from a fire hose or fire monitor (as seen in figure 7.1) is difficult a priori. While models exist at present, their accuracy outside the range of their calibration data is questionable. For example, if a model is calibrated for a certain nozzle, it is unlikely that the model would be accurate for a different nozzle, even with an identical internal flow system upstream of the nozzle.

Given how critical time to extinguishment is to total property and life loss, more accurately predicting how long it will take for a water jet to extinguish a fire is essential to more accurately assess risk. The development of an accurate model of the trajectory of a water jet would help to more accurately estimated fire risk where fire hoses or fire monitors are used. The specific scenarios where water jets are used to suppress fire are varied, from first responders who apply hose streams, to deck-mounted fire monitors on boats used to fight fires on the deck or even outside the boat. Fire monitors mounted on towers also are frequently used in fire protection scenarios, e.g., protection of pulpwood. There is also recent interest in fully autonomous fire suppression systems, where prediction of the trajectory from a fire nozzle is essential for fast targeting. The model developed in this work would prove useful in accessing and reducing fire risk in all of these scenarios.

¹An earlier version of the work in this chapter was published in a conference paper presented at ASME IMECE 2015 [TE15]. This chapter was completely rewritten using the conference paper as an outline to improve the presentation, correct errors, extend the theory, and improve the validation of the theory. Note that much of the notation has changed since then to be more consistent, be easier to understand, and simplify the results. I am the sole author; Prof. Ezekoye was included as an author on the conference paper for his advisory role.



Figure 7.1: Two fire monitors in use by the Portland Fire Department. Fire monitors can deliver 5000 GPM (~ 300 L/s) or more through nozzles up to and beyond 3 inches (~ 7 cm) in diameter, leading to maximum ranges of 200 meters or more. Photo from https://en.wikipedia.org/wiki/File:Deck_gun_on_American_fire_engine.jpg.

The scenario of interest is fire protection with large water jets, for example, hose streams and fire monitors. Consider a large water jet launched at a speed \bar{U}_0 and an angle θ_0 to the horizontal with the center of the nozzle of diameter d_0 at a height h_0 . The nozzle outlet is denoted with 0, so, e.g., the nozzle outlet diameter is d_0 . See figure 7.2 for an illustration of the problem. This jet gradually breaks up with distance from the nozzle, forming droplets which eventually reach the horizontal plane. The two quantities of interest are the surface water distribution (i.e., wetted area) and the maximum range R that the water jet projects water onto the horizontal plane. As show in figure 2.1, the surface water distribution is often biased towards R .

The basic nomenclature used for liquid jet breakup is shown in schematic in figure 2.1. In this frame the x axis is oriented streamwise. This is not the convention for the frame used in the trajectory models, where x is the distance from the nozzle outlet horizontally. The region of space over which liquid water is continuously connected to the nozzle outlet is called the jet core. The core flow (dark gray) starts being depleted of mass (on average) at

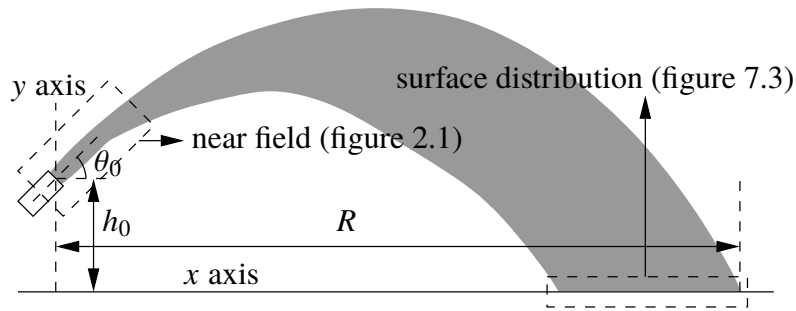


Figure 7.2: Basic trajectory nomenclature with firing angle θ_0 , firing height h_0 , and maximum range R .

the breakup onset location, $\langle x_i \rangle$. The core ends on average at the breakup length, $\langle x_b \rangle$; b in a subscript also refers to this location. Beyond x_b (the fluctuating breakup length rather than the average breakup length), liquid water exists only as discontinuous slugs and droplets. The lighter gray refers to the region where droplets exist.

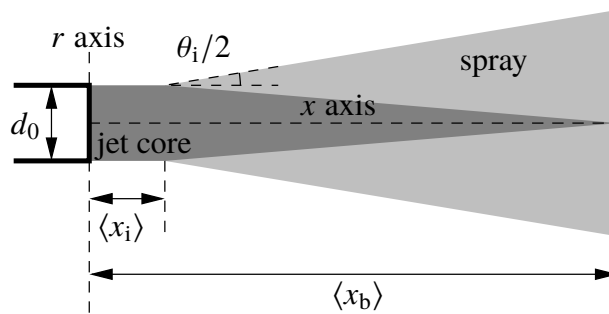


Figure 2.1: Jet breakup variables labeled on a schematic liquid jet. Coordinates are different from figure 7.2. d_0 is the nozzle outlet diameter, $\langle x_i \rangle$ is the average breakup onset location, θ_i is the spray angle, and $\langle x_b \rangle$ is the breakup length.

7.2 What influences the range of a water jet?

Because a variety of different factors influence the range and trajectory of a water jet, a review of these factors and what common models consider is needed. In this review, I emphasize that many previous models neglected important factors like the nozzle design. Selected functional dependencies of the problem studied in this work are shown in figure 1.1.

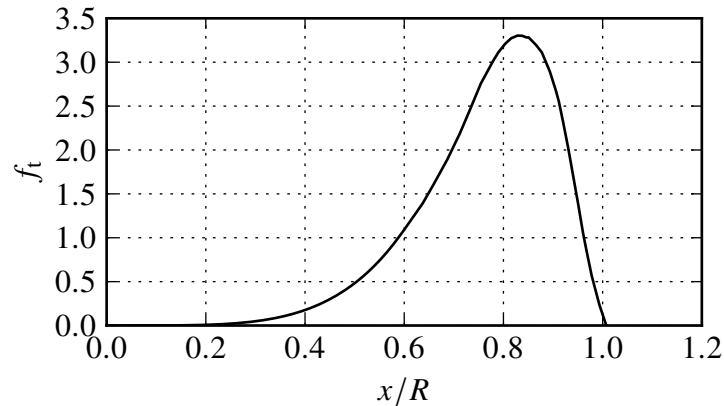


Figure 7.3: Surface water distribution example: probability density of water reaching distance x .

7.2.1 The water jet range anomaly

Water jet range can be estimated by assuming that droplets are emitted directly at the nozzle outlet at the velocity of the jet and that these droplets follow a ballistic trajectory with a known drag coefficient. I refer to this as the *instantaneous breakup* model. This model is known to severely underpredict the range of the jet. For example, Richards and Weatherhead [RW93, p. 284] report that the instantaneous breakup approach suggests that a 30 m/s jet at an angle of 24° producing a 5 mm droplet (presumably the nozzle outlet diameter) with a drag coefficient of 0.45 has a maximum range of 19.5 m, compared against 50 m found experimentally. I call this discrepancy the *range anomaly*.

Another common approach with large water jets is to assume that the jet experiences no drag. This is called the *dragless* approach. This approach over-predicts the range. For example, in the previously mentioned case, the dragless range is estimated to be about 68 m.

There also are empirical approaches to estimate range. The most simple empirical approaches are regression equations, which have been used by Lyshevskii [Lys62a] and Theobald [The81]. There also are computational models which use purely empirical drag models fitted to experimental data [Seg65; HO79; HLO85]. These drag models are inconsistent with known drag models for droplets. Models which select the droplet diameter distribution by matching range or water distribution data are similar, e.g., the model of

Fukui, Nakanishi, and Okamura [FNO80]. These models can lead to unrealistically large droplet diameters, as will be explained. Additionally, the accuracy of empirical models is questionable aside from the particular system they were calibrated for. This is particularly true given that some of the drag models used are dimensionally inhomogeneous. Smith et al. [Smi+08, p. 127R] note that empirical models typically require more calibration data than theoretical models for comparable accuracy.

Identifying the cause of the range anomaly is necessary to develop accurate models. I investigate three effects contributing to the range anomaly: air entrainment, jet breakup, and large droplets. Each effect exists in reality, but the relative contributions of each effect are not obvious at present.

7.2.1.1 Effect 1: Reduced drag due to air entrainment

One hypothesis is that the reduction in apparent drag is due primarily to air entrainment, as suggested by Murzabaeb and Yarin [MY85], Richards and Weatherhead [RW93, p. 284], and Grose [Gro99, p. 6]. The reasoning is that a higher entrainment velocity would reduce the velocity difference between the droplets and the surrounding gas flow (ΔU) and then decrease the drag ($F_d \propto \Delta U^2$) without necessarily changing the drag coefficients of the droplets themselves. The entrainment velocity is created through the coupling between the droplets (or the jet core) and the gas. This momentum coupling is essentially a gas phase momentum source term, much like the source term used to model buoyant plumes that will be discussed in § 7.3.1.5.

Air entrainment is not likely as simple as was just discussed. In contrast to the popular statement of the hypothesis, decreasing air entrainment might lead to an increase in range as suggested by Hoyt and Taylor [HT77a]. The logic here is that the momentum transfer from the jet to the air results in reduced range. The net effect of air entrainment may either be negligible or non-monotonic, i.e., a certain amount of air entrainment is ideal. Too little air entrainment leads to higher drag due to a larger velocity difference, while too much air entrainment requires high drag to occur in the first place.

Further, if increased air entrainment explains the range anomaly, then I might expect higher jet turbulence intensity to increase range. This is because as jet turbulence intensity increases, so does air entrainment [EME80; ME80]. And as air entrainment increases, the relative velocity between the droplets and air decreases, in turn decreasing drag and increasing range. However, increasing jet turbulence intensity is known to decrease range [RHM52; Oeh58]. This could be despite increased air entrainment helping the jet's range, as the jet's turbulence intensity would influence effect 2: increased drag due to jet breakup.

7.2.1.2 Effect 2: Reduced drag before jet breakup

The second hypothesis is that the reduced drag is a consequence of the jet breaking up gradually rather than more abruptly. The hypothesis that preventing breakup leads to increased range in a water jet has a long history [Sch37, p. 513; DiC+68, p. 16; HT77a, p. S253L; TT78, p. A4-56; The81, p. 1], though how jet coherence leads to longer range is not always stated. One possibility is that the “jet core”, sometimes called the “intact” or “coherent” part of the jet, experiences less drag than the droplets. This mechanism appears to have been first *recognized* in the efforts of Hatton and Osborne [HO79, p. 38L] to model fire hose streams in 1979, though they made no attempt to *model* the phenomena until 1985 [HLO85], after von Bernuth and Gilley [vBG84, p. 1438L] in 1984 independently developed a model for this effect for irrigation sprinklers. Others using this effect in their later models include Bragg [Bra85], Schottman and Vandergrift [SV86], Augier [Aug96], Kincaid [Kin96], and Zheng, Ryder, and Marshall [ZRM12].

Modeling this effect is much less common than the others, being neglected in the most popular models for jet sprinkler irrigation [CTM01]. This may be due in part to the paper of Seginer, Nir, and von Bernuth [SNvB91, p. 302], which suggested that the calibrated breakup length was negligible for the irrigation sprinklers they measured the trajectories of. Seginer, Nir, and von Bernuth measured neither droplet diameters or breakup lengths, however, so Seginer, Nir, and von Bernuth possibly selected droplet diameters which were unrealistic. This could have led to the incorrect conclusion that the breakup

length is negligible in the nozzles tested because the breakup length was calibrated, not measured. Another criticism of the approach is from Richards and Weatherhead [RW93, p. 284], who suggested that the breakup length is “hard to define” without elaborating.²

Additionally, this effect is the only one which can explain the long hypothesized effect that delaying the breakup of a water jet (i.e., increasing the breakup length) increases range³. The hypothesis that range increases if breakup is prevented has a long history and is the main design goal in fire nozzle design [RHM52; Oeh58; The81]. As evidence of this hypothesis, it is obvious that a fog nozzle would not have as long a range as a smooth bore (i.e., “solid” jet) nozzle. Additionally, the experiments of Theobald [The81] show that the range of a large water jet is roughly ordered by the breakup length, all else equal⁴. Unfortunately, Theobald’s experiments are the only I am aware of which quantitatively varied the breakup length independent of other variables, as opposed to qualitatively varying the breakup length by for example changing the nozzle design without measuring the breakup length.

The fog nozzle example also shows that air entrainment and jet breakup are coupled. Air entrainment would obviously be far stronger for a fine spray than an intact jet. As air entrainment is greater for finer sprays than intact jets, this would seem to suggest that longer breakup lengths would tend to reduce air entrainment and consequently increase drag. This highlights the suggestion that air entrainment could both increase or decrease drag depending on the situation.

Further, the earlier mentioned models treat the breakup length as a universal characteristic of water jet systems, neglecting the effects of nozzle geometry and the upstream flow (e.g., the effect of jet turbulence intensity). In other words, it is not sufficient

²The breakup length is defined clearly in § 2.2, and some additional comments on the definitions are made in § 4.2.

³It is likely that more vigorous breakup also leads to smaller average droplet diameters. But the maximum range is controlled primarily by the maximum droplet diameter in ballistic theories, and that does not appear to be influenced strongly by the average droplet diameter. The data is noisy, but it appears that the maximum droplet diameter is not a clear function of anything aside from the nozzle outlet diameter, d_0 . See the next subsection.

⁴Or roughly equal, as the droplet size varies in Theobald’s experiments.

to make a model with a nonzero breakup length or a nonzero length region where drag is reduced on the jet. Because the breakup length varies greatly between different nozzles and jet systems in general, models need to consider the variation in the breakup length.

Given the disconnect between nozzle design and trajectory models, there is a need to develop models which consider the effect of the nozzle geometry and upstream flow. A reductionist approach, examining the dependencies of specific parts of the problem rather than the whole is needed. Figure 1.1 illustrates the dependencies of each part of the problem and places each chapter of this dissertation in the context of each component of the problem. Previous models were essentially empirical (or at least “postdictive”), and consequently they were tied to the particular system they were calibrated to. A predictive trajectory model would not require calibration, and instead its input quantities could hypothetically be determined without a trajectory test, allowing a true prediction of the trajectory to be made. An example of this is determining the flow coefficient of a valve before implementing it into a flow system, rather than fitting the flow coefficient of the valve to the actual performance of the flow system. And while models can be calibrated to observed trajectories, there is little reason to believe calibrated models are accurate outside the range of the calibration data. I previously mentioned that simply changing the nozzle is likely to make a model inaccurate, as trajectory models typically have no nozzle specific input parameters. As another example, the model of Hatton, Leech, and Osborne [HLO85] is calibrated only for windless conditions. The drag on a cylinder positioned normal to the flow is quite different from that of a droplet or cylinder aligned with the direction of the flow. Consequently, the accuracy of this model should be suspect. A trajectory model based on more fundamental physics (including both nozzle/breakup and aerodynamic effects) would take such a distinction into account. If all of the relevant physics are contained in the trajectory model, and all of the model coefficients can be obtained without conducting a range test, then the model can make predictions.

Finally, it is not ideal to have a parameter which allows for mere *implicit* variation of the breakup length, or variation of the region where drag is reduced in more general. Using as a model input a parameter which can be measured independently of a trajectory test is preferred, as this would allow the model to be independently validated. Another problem is

that if a model uses a coefficient to change the length of a region with lower drag rather than the breakup length, it's not always obvious how that coefficient would change quantitatively if a nozzle geometry parameter were to change, but a breakup length model could handle this situation. Explicitly considering the breakup length avoids these issues.

7.2.1.3 Effect 3: Reduced drag due to large droplet sizes

Larger droplets have relatively less drag because their projected area to volume ratio is lower, increasing their inertia more than the corresponding increase in projected area. Fitting the droplet size distribution to range data is likely to overestimate the droplet sizes without consideration of jet coherence and air entrainment.

As assumption in previous analyses is that the largest droplets formed have a diameter D_{\max} equal to the nozzle outlet diameter, d_0 . This is not realistic. In both theory and experiment droplets larger than the nozzle can be formed. While the notion of a “droplet diameter” can be hard to define here because large droplets tend to be non-spherical [Haw96, p. 52], some general observations can be made. The diameter of a droplet formed by a laminar inviscid jet as found theoretically by Rayleigh [Ray78] (equation 2.4), about $1.89d_0$, has independently been proposed as the largest by Baljé and Larson [BL49, p. 2] and Dumouchel, Cousin, and Triballier [DCT05, p. 643R]. However, the experiments of Chen and Davis [CD64, p. 196] show the arithmetic average of the droplet diameter at the average breakup point (i.e., $\langle x_b \rangle$) downstream can vary from $1.46d_0$ to $4.30d_0$, clearly contradicting the suggestion that the Rayleigh diameter is the largest. The data of Miesse [Mie55, p. 1695] also has several cases where the droplet diameter was larger than the Rayleigh diameter. However, all D_{\max} measurements of Inoue [Ino63, p. 16.111] were less than the Rayleigh diameter. These results are highly variable, so ultimately, the most clear statement is that $D_{\max} = O(d_0)$ but larger than d_0 , D_{\max} varies, and it is unlikely that the D_{\max} is greater than $4.5d_0$ in practice.

Unlike the previous two effects, this effect is fairly well established and consequently will receive less attention in this chapter.

7.2.2 Other effects on the trajectory

7.2.2.1 Firing angle

Contrary to popular belief, the range of a large water jet is not typically maximized at a firing angle of $\theta_0 = 45^\circ$. It can be shown that the optimal firing angle is 45° only for dragless projectiles launched at a firing height h_0 of zero.

In practice, the optimal firing angle is typically found to be in the range of $30\text{--}35^\circ$ due largely to the effect of drag. The optimal angle increases to 45° as the pressure drops, which presumably results in less jet breakup and less drag [Fre89, p. 387; RHM52, fig. 20, p. 1171]. The optimal firing angle is a function of the jet Froude number, dimensionless breakup length, wind speed and direction, among other variables, so some inconsistency between studies is expected. The early study of Freeman [Fre89, p. 387] finds the optimal firing angle in still air to be 32° . Rouse, Howe, and Metzler [RHM52, pp. 1168–1171] find the optimal angle to be 30° in still air. Theobald [The81, p. 7L] suggests 35° for turbulent jets, and Comiskey and Yarin [CY18, p. 65] also suggests 35° for laminar jets.

7.2.2.2 Wind

Wind is known to have a strong effect on fire hose streams. Tests typically are done outdoors due to space restrictions. Experimentalists often wait to avoid wind [Fre89, p. 374]. Unfortunately, Rouse, Howe, and Metzler [RHM52, p. 1159] find that the winds are sufficiently calm outdoors only about 1% of the time. Theobald [The81, p. 7R] conducted their experiments in a large hangar to minimize the effects of wind. In a series of outdoor tests, Green [Gre71, p. 3] used two nozzles side-by-side to ensure that the wind conditions are roughly the same for both nozzles. Freeman [Fre89, p. 375] also used the same arrangement to compare two nozzles possibly in the presence of wind, but found this arrangement to be inappropriate for determining the range of a single nozzle due to a roughly equal increase of the range of each jet from the extra air entrainment. (The arrangement of tests into similar groups is called “blocking” in the design of experiments literature.) In the multi-nozzle setup, any differences observed between the jets could be attributed solely to other changes

made — Green was interested in the addition of polymers, but it could be a nozzle design change as well.

There is very little research on the effect of wind on the entire trajectory large water jets. There is a very large amount of research on the “jet-in-cross-flow” configuration, and in particular the effect of the cross-flow/wind on the breakup and trajectory of the jet relatively near the nozzle, e.g., see the study and review of Birouk, Nyantekyi-Kwakye, and Popplewell [BNP11] for subsonic cross-flows. The water jet trajectory problem requires examination of areas farther downstream, unfortunately. The jet-in-cross-flow studies also suffer from a problem the trajectory studies suffer from: few (if any) experiments vary the breakup length independent of other variables. This is even more complicated than the windless trajectory case as the wind also changes the breakup length. Improving jet coherence has been hypothesized to improve wind resistance of water jets [Gre71, p. 1].

The jet shape influences how much wind resistance the jet has, with “hollow core” jets produced by a combination nozzle being more susceptible to find than “solid” jets [For91, p. 253], to use terminology from the fire protection literature. This work focuses primarily on “solid” jets. (In principle hollow core jets can be handled in this framework if the breakup length and droplet size distribution are known.)

Because one of the effects of wind is to increase the amount of drag, the optimal firing angle in wind is expected to be lower than that without wind. Cousins and Stewart [CS30, p. 2] observed that the effects of wind were strongest at larger firing angles. The optimal firing angle under windy conditions has been informally observed in practice to be about 10° in roughly 15 m/s wind [PG71, p. 2]. Simulations performed by von Bernuth [vBer88] suggest the optimal firing angle can be lower than 5° in winds greater than 8 m/s. Another potential cause of the reduction in the optimal firing angle is the existence of the atmospheric boundary layer. The closer the jet is to the ground, the lower the wind velocity it experiences.

7.2.2.3 Firing height

The effect of the firing height h_0 on the trajectory is characterized through the height Froude number, $Fr_{h_0} \equiv \bar{U}_0^2 / (gh_0)$. In still air, the range increases as h_0 increases, or equivalently, as Fr_{h_0} decreases.

If there is no drag, the optimal firing angle can be shown to increase to 45° as Fr_{h_0} increases and decrease to 0° as Fr_{h_0} decreases.

Typically, Fr_{h_0} is small because the velocities involved in the water jet trajectory problem are relatively large. However, the effect of Fr_{h_0} is not always negligible, and as a consequence I'll be including a non-zero firing height in this work.

7.2.2.4 Jet velocity or pressure

The range of a water jet increases as the jet velocity (or equivalently, pressure) is increased, up to a point. After that point, the range will no longer increase as velocity increases [RHM52, p. 1168; Eut57]. The precise reasons for this are unclear, though a change in the regime of the jet from the turbulent surface breakup regime to the atomization regime is a possibility. See chapter 3 for more information on the regimes of a liquid jet.

7.3 Analytical theory and validation

This chapter presents an approximate analytical theory of water jet *maximum range* [TE15] which I call “multi-stage theory”. To summarize the theory, a fluid particle travels from the nozzle initially in the “intact” part of the jet. Intact means that the jet has not yet broken into droplets. Jet breakup occurs at a known distance from the nozzle (the breakup length, $\langle x_b \rangle$), after which the fluid particle is a droplet. The model has different drag models for the intact and droplet stages of the jet. Of the effects mentioned in § 7.2.1, the model considers the intact portion of the jet, air entrainment, and droplet size, however, the air entrainment model is rudimentary.

That the nozzle design can strongly affect the range of a water jet is well known.

But until the model presented in this chapter was developed, this fact was not completely reflected in a model beyond the effect of the nozzle design on the droplet size. The droplet size is not a typically discussed effect among nozzle designers. Nozzle designers have an intuitive idea that making breakup occur farther downstream increases range, and it is this effect which I wanted to implement in a model.

It is not sufficient for a model to merely *consider* breakup. One could argue that all instantaneous breakup models consider breakup. Models which consider breakup but assume that the breakup process is universal (e.g., constant breakup length), and not influenced by the nozzle design, are unacceptable.

A related goal of the model is to not require range tests to credibly estimate the range and water distribution. All of the parameters in the model can be measured without measuring range. For example, the breakup length can be measured photographically or through electrical conductivity. The droplet size distribution (and characteristic diameters like D_{\max} and D_{32}) can be measured through many standard techniques. The parameters in the model are not purely for tuning the model. They have physical meanings and ideally will match those measured experimentally. Additionally, leaving these breakup parameters as inputs to the trajectory model allows the use of separate jet breakup models. The trajectory model can use improved jet breakup models developed in the future without modification. This approach also gives confidence to nozzle designers that changes in the breakup parameters (as controlled by the nozzle design) will have the desired effect on the trajectory.⁵

7.3.1 Submodels

7.3.1.1 Drag on the intact jet

For fluid particles before jet breakup occurs, the drag is treated as zero. This is not strictly true, but is the approximation I'll use in this work. For laminar jets

⁵While in practice I calibrate the maximum droplet size to the data here, this can be viewed as converting a real non-spherical large "droplet" to a spherical droplet of diameter D_{\max} with equivalent drag.

($621 \leq \text{Re}_{\ell_0} \leq 1289$), Comiskey and Yarin [CY18] measured and correlated the (jet length) average skin friction coefficient with the equation $\overline{C}_f = 5\text{Re}_{\ell_0}^{-1/2}$. The cases of interest are turbulent, however, so the applicability of this relationship beyond the Reynolds number limits of the experiment are unknown. The correlation suggests that the drag on high Reynolds number jets is likely low.

Even if the drag in the direction of the jet's motion is negligible, the drag from wind is not. In this model, wind is neglected entirely for simplicity.

7.3.1.2 Jet breakup location

After breakup occurs, droplets are formed. The breakup location can vary greatly for each droplet, from as small as x_i , where breakup is first initiated, to as high as x_b , where the jet core finally breaks. As a first approximation, the model assumes that all breakup occurs at $\langle x_b \rangle$. As droplet mass flux increases greatly with distance from the nozzle [SDF02, p. 445–446, fig. 10], the droplet volume is expected to mostly come from near the end, x_b .

Additionally, the standard deviation of the breakup length, σ_b , is a relatively small fraction of the total breakup length. This would indicate that the end of breakup is reasonably well approximated as occurring at the average breakup length, $\langle x_b \rangle$. Defining the coefficient of variation of the breakup length $C_{\sigma_b} \equiv \sigma_b / \langle x_b \rangle$, I find that the available data [Phi73; YO78] is well represented by $C_{\sigma_b} = 0.1291 \pm 0.0019$. This appears to be independent of the nozzle design, but likely applies only for turbulent surface breakup and atomization regimes as the proportionality seems to fail at lower velocities [LDL96, fig. 6–7]. Additionally, the single DNS data point of Agarwal and Trujillo [AT18, fig. 17] returns $C_{\sigma_b} = 0.0847$, which is lower than the experiment, likely because the jet is initially laminar (a different regime; see chapter 3). Figure 7.4 shows a cumulative distribution plot of the instantaneous breakup length x_b divided by the average breakup length $\langle x_b \rangle$ for jets produced from converging nozzles, abrupt contraction nozzles, and pipe nozzles. A straight line corresponds to a normal distribution in these coordinates; the available data appears to be well described by normal distributions. The slope determines the standard deviation.

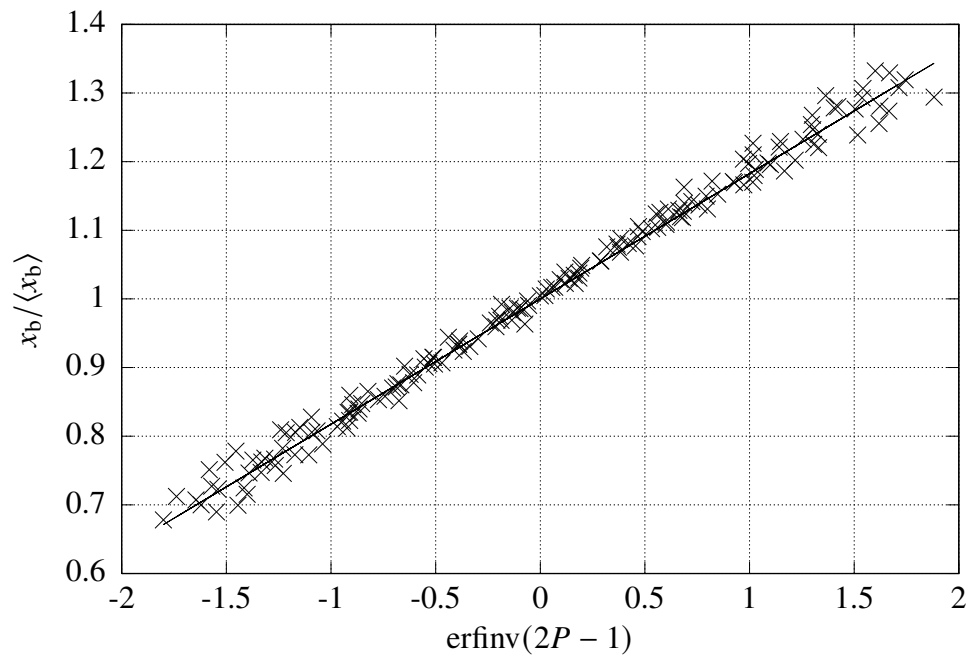


Figure 7.4: A cumulative distribution plot of the instantaneous breakup length normalized by the average breakup length. In these coordinates, a normal distribution is a straight line. Experimental data from Phinney [Phi73] and Yanaida and Ohashi [YO78].

7.3.1.3 Maximum droplet diameter and droplet breakup

The maximum droplet diameter is treated as constant. Breakup of droplets is neglected in this chapter for simplicity. Large droplets are unstable and will break up into smaller droplets [LM17, p. 19], and I believe the neglect of this feature to be the largest source of uncertainty out of those I mentioned. However, existing models for droplet breakup are not known to be particularly accurate and may not improve the accuracy much.

The particle mass does not need to be defined for the jet core in this model, but it does need to be defined for the droplet stage. This requires knowledge of the droplet diameter. As larger droplets travel farther, the maximum range corresponds to the maximum droplet diameter, D_{\max} . As mentioned in § 7.2.1.3, the maximum droplet diameter is not very precisely known aside that it's $\mathcal{O}(d_0)$. Consequently, the maximum droplet diameter will be chosen to fit the data later in this chapter.

7.3.1.4 Droplet drag

The droplet drag model is standard quadratic drag with a constant drag coefficient, which is a commonly used model. The droplet Reynolds number is approximately (considering the velocity constant and neglecting air entrainment) $D_{\max}\overline{U}_0/\nu_g$ which is $\mathcal{O}(10^4)$ in the validation experiments, before the drag crisis typically occurs, where the drag coefficient for a solid sphere is relatively constant [MYO05, p. 526]. Change of the droplet drag coefficient for any reason (Reynolds number variation, droplet shape variation, or other reasons) is neglected in this chapter for simplicity. Loth [Lot08, p. 524L] suggests that $C_d = 0.42$ for a solid spherical particle at high Reynolds number, within 6%, and this is the value used.

7.3.1.5 Air entrainment

The air entrainment model used in this work is simplistic and will only act to increase range, even though there are reasons to believe that air entrainment can decrease range as well — see § 7.2.1.1. In buoyant plume theory [MTT56], an entrainment coefficient

is defined. The entrainment coefficient relates the velocity of the plume centerline to the entrainment velocity. The entrainment coefficient is essentially empirical, and can be viewed as analogous to the (also essentially empirical) turbulent viscosity used in elementary turbulent jet theory [Pop00, pp. 118–122].

Due to differences between the jet and buoyant plume cases, a similar but not identical definition of the entrainment coefficient α was developed:

$$\vec{U}_g \equiv \alpha \vec{U}_d. \quad (7.1)$$

The droplets and gas phase can occupy the same location at different times, so in a time averaged model it could be reasonable to use equation 7.1 along the centerline of the jet.

The experimental measurements of air flow in a spray of Heskestad, Kung, and Todtenkopf [HKT76, figs. 4–6] suggest that $\alpha = 0.1$ is a reasonable approximation to one significant figure at the jet centerline. Given that the spray was much finer in Heskestad, Kung, and Todtenkopf’s experiment than the more coherent jets studied in this work, I’d expect the entrainment coefficient to be lower than Heskestad, Kung, and Todtenkopf’s, perhaps around 0.05. This is the value used in this work.

A constant entrainment coefficient is a crude approximation. I expect the local entrainment coefficient to vary with the spatial coordinate, Reynolds number, Weber number, and density ratio, if not other variables. However, this approximation is expected to be reasonable enough to roughly determine the sensitivities of the problem. In the future a model for the entrainment coefficient as a function of the droplet drag coefficients and other variables could be developed, generalizing the model further.

7.3.2 Maximum height of a water jet fired vertically

Before focusing on the problem of the full trajectory of a water jet, I’ll focus on the simpler problem of the maximum height of a jet fired vertically without wind. Decorative fountains are often fired vertically, and the scenario is also relevant to fighting high-rise fires.

Breakup occurs at a distance $\langle x_b \rangle$ (the breakup length) above the nozzle, which is the origin ($Y = 0$). Before breakup, the jet follows a dragless trajectory. After breakup, the jet is composed of spherical droplets of varying diameters. These droplets are assumed to be not interacting, so they can overlap without collisions or coalescence. As discussed, these droplets have constant drag coefficients. I also only compute the trajectory for a droplet of size D_{\max} as I am interested in h , the maximum height. Wind is neglected here. As stated, air entrainment will be handled in a crude fashion with a constant entrainment coefficient.

The vertical coordinate Y_j will be used for the jet centerline. When $Y_j < \langle x_b \rangle$, the equation of motion of the jet is:

$$\frac{d^2 Y_j}{dt^2} = \frac{dV_j}{dt} = -g, \quad (7.2)$$

where the jet core velocity is V_j .

Equation 7.2 can be solved to obtain the height and velocity as a function of time. These solutions are

$$\frac{dY_j}{dt}(t) = V_j = \bar{U}_0 - gt, \quad (7.3)$$

$$Y_j(t) = \bar{U}_0 t - \frac{1}{2}gt^2, \quad (7.4)$$

where \bar{U}_0 is the jet bulk velocity⁶. When the breakup length $\langle x_b \rangle$ is less than the maximum possible height H , I'll model the jet as breaking up into droplets instantaneously at $Y_j = \langle x_b \rangle$. At the breakup point the velocity is $V_b = \sqrt{\bar{U}_0^2 - 2g\langle x_b \rangle}$.

For non-dimensionalization, it's useful to normalize by the maximum possible height a jet could obtain to create a "jet efficiency" that is bounded between 0 and 1. This height can be found from equation 7.4, because in the best case no breakup occurs. The

⁶Note that in the *water jet trajectory* coordinate system, Y is the vertical coordinate, while in the *jet breakup* coordinate system, x is the nozzle axis coordinate. Consequently, the jet bulk velocity \bar{U}_0 in the x direction of the nozzle is also in the Y direction of the trajectory frame. Additionally, as the water jet trajectory computed here is essentially an ensemble-averaged quantity, rather than writing $\langle Y \rangle$, I'll write Y for brevity, using the capitalization as an implied average here. A j subscript will be used for the jet core trajectory, and a d subscript will be used for the droplet trajectory.

maximum possible height is $H = \bar{U}_0^2/(2g)$, assuming a uniform velocity profile. The real height the jet obtains is h . Consequently, the definition of the jet height efficiency is

$$\eta_h \equiv \frac{h}{H} = \frac{2gh}{\bar{U}_0^2}. \quad (7.5)$$

(This definition was first used by Arato, Crow, and Miller [ACM70, p. 2].)

Applying simple Newtonian dynamics, the equation of motion for a particular droplet (after jet breakup, so Y_j changes to Y_d) is

$$m_d \frac{dV_d}{dt} = -m_d g - \frac{1}{2} \rho_g C_d A_d (V_d - V_g)^2, \quad (7.6)$$

where m_d is the mass of the droplet, V_d is the droplet velocity, and V_g is the velocity of the gas immediately around the droplet.

Then, approximating the droplets as spherical, I obtain

$$\frac{\pi}{6} \rho_\ell D^3 \frac{dV_d}{dt} = -\frac{\pi}{6} \rho_\ell D^3 g - \frac{1}{2} \rho_g C_d \frac{\pi}{4} D^2 (V_d - V_g)^2. \quad (7.7)$$

Equation 7.7 can be used to calculate the trajectory for any droplet size D in the entire droplet size distribution $f_D(D)$. My interest in this example is in the maximum height obtained by the jet, which is obtained only for the largest droplets of diameter D_{\max} . The equation can be further simplified through the use of a constant entrainment coefficient. If I define the entrainment coefficient α through the equation $V_g = \alpha V_d$, then $V_d - V_g = (1 - \alpha)V_d$. With these modifications, equation 7.7 is now

$$\frac{\pi}{6} \rho_\ell D_{\max}^3 \frac{dV_d}{dt} = -\frac{\pi}{6} \rho_\ell D_{\max}^3 g - \frac{1}{2} \rho_g C_d \frac{\pi}{4} D_{\max}^2 (1 - \alpha)^2 V_d^2. \quad (7.8)$$

Non-dimensionalizing this result with $\tau \equiv t/(V_b/g)$ and $V_d^* \equiv V_d/V_b$ leads to

$$\frac{dV_d^*}{d\tau} = -1 - \frac{3}{4} \frac{C_d}{\rho_\ell/\rho_g} \frac{(1 - \alpha)^2}{D_{\max}/d_0} Fr_0 (V_b^*)^2 (V_d^*)^2, \quad (7.9)$$

where

$$V_b^* \equiv \frac{V_b}{U_0} = \sqrt{1 - \frac{2\langle x_b \rangle / d_0}{Fr_0}}. \quad (7.10)$$

For simplicity I'll define a reduced drag coefficient:

$$C_d^* \equiv \frac{3}{2} \frac{C_d}{\rho_\ell / \rho_g} \frac{(1 - \alpha)^2}{D_{\max} / d_0}, \quad (7.11)$$

so the non-dimensional equation of motion can be written as

$$\frac{dV_d^*}{d\tau} = -1 - \frac{1}{2} C_d^* Fr_0 (V_b^*)^2 (V_d^*)^2, \quad (7.12)$$

or after defining $\widehat{C}_d \equiv C_d^* Fr_0 (V_b^*)^2$,

$$\frac{dV_d^*}{d\tau} = -1 - \frac{1}{2} \widehat{C}_d (V_d^*)^2. \quad (7.13)$$

Separating variables and integrating equation 7.13 from time τ_b (when the breakup starts, so $V_d(\tau_b) = V_b$) returns

$$\int_{\tau_b}^{\tau} d\widehat{\tau} = \int_1^{V_d^*} \frac{-d\widehat{V}_d^*}{1 + \frac{1}{2} \widehat{C}_d (\widehat{V}_d^*)^2}, \quad (7.14)$$

$$(\tau - \tau_b) = \frac{\text{atan}\left(\sqrt{\widehat{C}_d/2}\right) - \text{atan}\left(V_d^* \sqrt{\widehat{C}_d/2}\right)}{\sqrt{\widehat{C}_d/2}}, \quad (7.15)$$

which can be solved for V_d^* :

$$V_d^* = \frac{\tan\left[\text{atan}\left(\sqrt{\widehat{C}_d/2}\right) - (\tau - \tau_b) \sqrt{\widehat{C}_d/2}\right]}{\sqrt{\widehat{C}_d/2}}. \quad (7.16)$$

Equation 7.16 can now be integrated to obtain the maximum height. First, it is necessary to determine at what dimensionless time, τ_{top} the maximum height is obtained. The vertical

velocity $V_d^* = 0$ when $\tau = \tau_{\text{top}}$, so equation 7.16 can be solved to find that

$$\tau_{\text{top}} - \tau_b = \frac{\text{atan}\left(\sqrt{\widehat{C}_d/2}\right)}{\sqrt{\widehat{C}_d/2}}. \quad (7.17)$$

Now the maximum height can be found by integrating from the breakup point to the maximum height:

$$h = \langle x_b \rangle + \int_{t_b}^{t_{\text{top}}} V_d \, dt = \langle x_b \rangle + \frac{V_b^2}{g} \int_{\tau_b}^{\tau_{\text{top}}} V_d^* \, d\widehat{\tau}, \quad (7.18)$$

which leads to (after simplifying via trigonometric identities)

$$h = \langle x_b \rangle + \frac{V_b^2}{g} \frac{\ln(\widehat{C}_d/2 + 1)}{\widehat{C}_d}. \quad (7.19)$$

The height efficiency η_h can be obtained from equation 7.19 by applying its definition (equation 7.5) and simplifying using the fact that $\widehat{C}_d \equiv C_d^* \text{Fr}_0 (V_b^*)^2$:

$$\eta_h = \frac{2\langle x_b \rangle/d_0}{\text{Fr}_0} + \frac{2}{C_d^* \text{Fr}_0} \ln \left[\frac{C_d^*}{2} \left(\text{Fr}_0 - \frac{2\langle x_b \rangle}{d_0} \right) + 1 \right]. \quad (7.20)$$

The maximum height in physical coordinates is

$$h = \langle x_b \rangle + \frac{d_0}{C_d^*} \ln \left[\frac{C_d^*}{2} \left(\text{Fr}_0 - \frac{2\langle x_b \rangle}{d_0} \right) + 1 \right]. \quad (7.21)$$

Another possible non-dimensionalization which simplifies some results uses h^* (h -star), defined as

$$h^* \equiv \frac{C_d^* h}{d_0}. \quad (7.22)$$

The h^* equation then is

$$h^* = \frac{C_d^* \langle x_b \rangle}{d_0} + \ln \left[\frac{C_d^*}{2} \left(\text{Fr}_0 - \frac{2\langle x_b \rangle}{d_0} \right) + 1 \right]. \quad (7.23)$$

For convenience, the reduced drag coefficient is

$$C_d^* \equiv \frac{3}{2} \frac{C_d}{\rho_\ell / \rho_g} \frac{(1 - \alpha)^2}{D_{\max} / d_0}. \quad (7.11)$$

As a check on equation 7.20, consider the case where the reduced drag coefficient C_d^* goes to zero, which should cause the jet efficiency to be one. This is not obviously seen in equation 7.20 analytically due to the $2/C_d^*$ term, so I'll use the Taylor series for $\ln(x + 1)$,

$$\ln(x + 1) = \sum_{n=1}^{\infty} \frac{(-1)^{n+1}}{n} x^n, \quad (7.24)$$

and compute the limit:

$$\begin{aligned} \lim_{C_d^* \downarrow 0} \eta_h &= \frac{2\langle x_b \rangle / d_0}{Fr_0} + \lim_{C_d^* \downarrow 0} \sum_{n=1}^{\infty} \frac{(-1)^{n+1}}{n} \left(\frac{C_d^* Fr_0}{2} \right)^{n-1} \left(1 - \frac{2\langle x_b \rangle / d_0}{Fr_0} \right)^n, \quad (7.25) \\ &= \frac{2\langle x_b \rangle / d_0}{Fr_0} + 1 - \frac{2\langle x_b \rangle / d_0}{Fr_0} \end{aligned}$$

$$+ \lim_{C_d^* \downarrow 0} \sum_{n=2}^{\infty} \frac{(-1)^{n+1}}{n} \left(\frac{C_d^*}{2} \right)^{n-1} \left(1 - \frac{2\langle x_b \rangle / d_0}{Fr_0} \right)^n \quad (7.26)$$

$$= 1. \quad (7.27)$$

Every term aside from the $n = 1$ term was proportional to C_d^* , so those terms are zero in the limit. The $n = 1$ term does not contain C_d^* , but it does contain some breakup length terms which cancel each other out, returning $\eta_h = 1$ in the limit.

The case where the jet does not breakup before reaching its peak ($\langle x_b \rangle = H$) returns $2\langle x_b \rangle / d_0 = Fr_0$. Then

$$\eta_h(\langle x_b \rangle = H) = 1 + \frac{2}{C_d^*} \ln 1 = 1, \quad (7.28)$$

as is expected because the jet experiences no drag before breakup in this model.

In the earlier conference paper version of this work [TE15], equation 7.20 was favorably compared against experimental data from Arato, Crow, and Miller [ACM70].

However, Arato, Crow, and Miller's experiments were conducted outdoors, leading to a large spread in the data. Additionally, Arato, Crow, and Miller's data was presented in a way which makes determining details of the nozzles used impossible, requiring making unjustified assumptions. Consequently, new experiments are required to properly validate equation 7.20. Some new vertical jet experiments were conducted indoors for this dissertation but were deemed incomplete and preliminary. These experiments will be published in the future when complete.

7.3.3 Maximum range of a water jet fired approximately horizontally

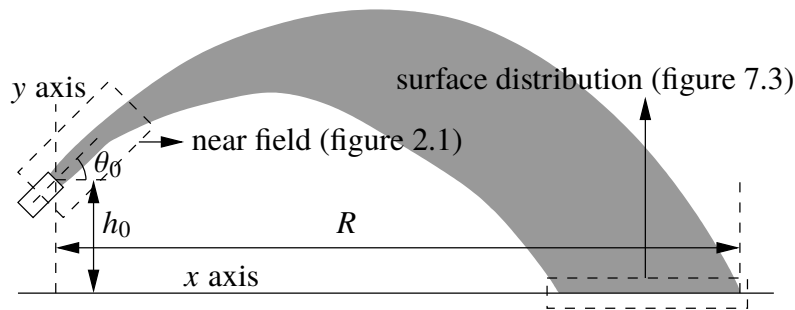


Figure 7.2: Basic trajectory nomenclature with firing angle θ_0 , firing height h_0 , and maximum range R .

The more general trajectory case is considerably more complex, as can be seen in figure 7.2. The general outline of the analytical solution of the trajectory case is the same as that of the vertical height case. First, the trajectory of the jet's core (X_j and Y_j) is computed without wind, then the trajectory of the droplets after breakup (X_d and Y_d) is computed. As in figure 7.2, X is horizontal and Y is vertical.

7.3.3.1 Dragless jet core trajectory

The equations of motion and initial conditions for the jet's core (dragless) are

$$\begin{aligned} \frac{d^2 X_j}{dt^2} &= \frac{dU_j}{dt} = 0, & \frac{d^2 Y_j}{dt^2} &= \frac{dV_j}{dt} = -g, \\ X_j(0) &= 0, & Y_j(0) &= h_0, \end{aligned}$$

$$\frac{dX_j}{dt}(0) = U_j = \bar{U}_0 \cos \theta_0, \quad \frac{dY_j}{dt}(0) = V_j = \bar{U}_0 \sin \theta_0, \quad (7.29)$$

where θ_0 is the firing angle, h_0 is the firing height, and, as before, g is the acceleration due to gravity and \bar{U}_0 is the jet bulk velocity. These equations have the solutions

$$X_j(t) = \bar{U}_0 \cos(\theta_0) t, \quad (7.30)$$

$$Y_j(t) = \bar{U}_0 \sin(\theta_0) t - \frac{1}{2} g t^2 + h_0. \quad (7.31)$$

To non-dimensionalize the range as an efficiency like in the vertical jet case, it is necessary to first find the maximum possible range in the dragless case given a fixed firing height h_0 (setting the firing angle θ_0 to the optimal value). This derivation is tedious and omitted for brevity⁷. Using the maximum possible range, the range efficiency is

$$\eta_R \equiv \frac{R}{R_{\text{opt}}} = \frac{Rg}{\bar{U}_0^2} \sqrt{\frac{\text{Fr}_{h_0}}{\text{Fr}_{h_0} + 2}}. \quad (7.32)$$

7.3.3.2 Droplet trajectory after breakup

The breakup length in the trajectory case needs to be generalized to consider the curvature of the trajectory. There are two main options: breakup occurs where the arclength of the jet equals the breakup length $\langle x_b \rangle$, or that breakup occurs at the breakup time $\langle t_b \rangle \equiv \langle x_b \rangle / \bar{U}_0$. Both of these reduce to breakup occurring a distance $\langle x_b \rangle$ along the nozzle if the trajectory is straight. However, the breakup time specification is mathematically simpler and will be chosen for that reason.

The breakup locations X_b and Y_b can be computed from equations 7.30 and 7.31:

$$X_b \equiv X_j(\langle t_b \rangle) = \bar{U}_0 \cos \theta_0 \frac{\langle x_b \rangle}{\bar{U}_0} = \langle x_b \rangle \cos \theta_0, \quad (7.33)$$

$$Y_b \equiv Y_j(\langle t_b \rangle) = \bar{U}_0 \sin \theta_0 \frac{\langle x_b \rangle}{\bar{U}_0} - \frac{1}{2} g \left(\frac{\langle x_b \rangle}{\bar{U}_0} \right)^2 + h_0,$$

⁷Part of the proof can be found in a Mathematics Stack Exchange post [Pic15].

$$= \langle x_b \rangle \sin \theta_0 - \frac{g}{2} \left(\frac{\langle x_b \rangle}{\bar{U}_0} \right)^2 + h_0. \quad (7.34)$$

And the velocities at breakup are

$$U_b \equiv U_j(\langle t_b \rangle) = \bar{U}_0 \cos \theta_0, \quad (7.35)$$

$$V_b \equiv V_j(\langle t_b \rangle) = \bar{U}_0 \sin \theta_0 - \frac{g \langle x_b \rangle}{\bar{U}_0}. \quad (7.36)$$

The position and velocity of the jet at breakup will be used as the initial conditions for the droplets after breakup. Similar to the vertical height case, the droplet stage of the trajectory has the equation of motion

$$m_d \frac{d\vec{U}_d}{dt} = -m_d \vec{g} - \frac{1}{2} \rho_g C_d A_d \left\| \vec{U}_d - \vec{U}_g \right\| (\vec{U}_d - \vec{U}_g), \quad (7.37)$$

where $\vec{U}_d = U_d \hat{i} + V_d \hat{j}$ is the droplet velocity vector, \vec{U}_g is the air velocity vector, and the remainder of the terms are the same as in the vertical jet case. The air entrainment model $\vec{U}_g \equiv \alpha \vec{U}_d$ can be applied to this case as before.

In the trajectory case it is more convenient to non-dimensionalize by the jet bulk velocity \bar{U}_0 instead of the breakup velocity $|\vec{U}_b|$, as was done in the vertical jet case. Consequently, here I define

$$\tau \equiv \frac{t}{\bar{U}_0/g}, \quad (7.38)$$

$$\vec{U}_d^* \equiv \frac{\vec{U}_d}{\bar{U}_0}, \text{ and} \quad (7.39)$$

$$\vec{X}_d^* \equiv \frac{\vec{X}_d}{\bar{U}_0^2/g}, \quad (7.40)$$

then non-dimensionalize the equation of motion to obtain

$$\frac{d\vec{U}_d^*}{d\tau} = -\hat{j} - \frac{3}{4} \frac{C_d}{\rho_\ell/\rho_g} \frac{(1-\alpha)^2}{D_{\max}/d_0} \text{Fr}_0 \left\| \vec{U}_d^* \right\| \vec{U}_d^*, \quad (7.41)$$

which, after introducing the reduced drag coefficient (equation 7.11) is simplified to

$$\frac{d\vec{U}_d^*}{d\tau} = -\hat{j} - \frac{1}{2}C_d^*Fr_0\left\|\vec{U}_d^*\right\|\vec{U}_d^*. \quad (7.42)$$

Now, for simplicity, let's define

$$C_d^\circ \equiv C_d^*Fr_0 \quad (7.43)$$

so that

$$\frac{d\vec{U}_d^*}{d\tau} = -\hat{j} - \frac{1}{2}C_d^\circ\left\|\vec{U}_d^*\right\|\vec{U}_d^*. \quad (7.44)$$

The equations of motion of a particle experiencing quadratic drag in two dimensions (like equation 7.44) are not known to have analytical solutions⁸. Fortunately, a small firing angle approximation called the “flat fire” approximation (found in this work to be accurate for firing angles less than 35°) can be applied. This approximation is well known in the ballistics literature [McC12, § 5.3], but has not been applied to the trajectory of water jets before this work. In the flat fire approximation the droplet velocity magnitude $\left\|\vec{U}_d\right\|$ is assumed equal to U_d because if the firing angle θ_0 is small then V_d is small. Consequently, the approximate system of ODEs is

$$\frac{dU_d^*}{d\tau} = -\frac{1}{2}C_d^\circ(U_d^*)^2, \quad (7.45)$$

$$\frac{dV_d^*}{d\tau} = -1 - \frac{1}{2}C_d^\circ U_d^* V_d^*. \quad (7.46)$$

As the drag force in the flat fire approximation is smaller than reality, this approximation will overpredict the range of the jet, with larger errors for larger firing angles. Note

⁸There is a subtle math error which has allowed some water jet trajectory researchers to develop what they believe to be exact solutions to the quadratic drag equations. Kawakami [Kaw71, p. 178L] and Lorenzini [Lor04, p. 3] demonstrate this error. Using Lorenzini's notation, the drag law can be written as $\vec{F}_d = -k\vec{U}_d^2$. This notation is ambiguous as the vector product is not defined clearly. Unfortunately this ambiguity leads the author to write the drag laws for each direction incorrectly. The vector drag law would be more correctly written as $\vec{F}_d = -k\left\|\vec{U}_d\right\|\vec{U}_d = -k\sqrt{U_d^2 + V_d^2}(U_d\hat{i} + V_d\hat{j})$. This notation is unambiguous and shows that the x and y directions are coupled. Instead, Lorenzini uses $\vec{U}_d^2 = U_d^2\hat{i} + V_d^2\hat{j}$, which is false. If this error is instead viewed as an approximation, this is still not acceptable as if the x velocity were large, then the y term would also need to be at least that large, but Lorenzini's specification does not allow that.

that because this is an approximation, it can not be used for quantitative verification of CFD software packages, though it may be useful as a qualitative check that the CFD software is close to the flat fire solution when expected to be.

Initial conditions are needed to solve the non-dimensional equations of motion (equations 7.45 and 7.46). The non-dimensional initial conditions are

$$X_b^* \equiv X_d^*(\tau_b) = \frac{g\langle x_b \rangle}{\bar{U}_0^2} \cos \theta_0 = \frac{\langle x_b \rangle / d_0}{Fr_0} \cos \theta_0, \quad (7.47)$$

$$Y_b^* \equiv Y_d^*(\tau_b) = \frac{\langle x_b \rangle / d_0}{Fr_0} \sin \theta_0 - \frac{1}{2} \left(\frac{\langle x_b \rangle / d_0}{Fr_0} \right)^2 + \frac{1}{Fr_{h_0}}, \quad (7.48)$$

$$U_b^* \equiv U_d^*(\tau_b) = \cos \theta_0, \quad (7.49)$$

$$V_b^* \equiv V_d^*(\tau_b) = \sin \theta_0 - \frac{\langle x_b \rangle / d_0}{Fr_0}. \quad (7.50)$$

Using these initial conditions, the solutions are

$$U_d^* = \frac{U_b^*}{\frac{1}{2} C_d^\circ U_b^* \tau + 1}, \quad (7.51)$$

$$V_d^* = - \left(\frac{\frac{1}{2} C_d^\circ U_b^* \tau + 1}{C_d^\circ U_b^*} \right) + \frac{1}{\frac{1}{2} C_d^\circ U_b^* \tau + 1} \left(V_b^* + \frac{1}{C_d^\circ U_b^*} \right), \quad (7.52)$$

$$X_d^* = \frac{2 \ln \left(\frac{1}{2} C_d^\circ U_b^* \tau + 1 \right)}{C_d^\circ} + X_b^*, \quad (7.53)$$

$$Y_d^* = - \left(\frac{\frac{1}{2} C_d^\circ U_b^* \tau + 1}{C_d^\circ U_b^*} \right)^2 + \frac{2}{C_d^\circ U_b^*} \left(V_b^* + \frac{1}{C_d^\circ U_b^*} \right) \ln \left(\frac{1}{2} C_d^\circ U_b^* \tau + 1 \right) + \frac{1}{(C_d^\circ U_b^*)^2} + Y_b^*. \quad (7.54)$$

A sketch of the solution procedure will be provided for brevity. Equation 7.45 is a first-order autonomous ODE which can readily be solved by separation of variables and direct integration. Once equation 7.45 is solved, the result can be substituted into equation 7.46. Then equation 7.46 can be solved after applying the change of variables $\xi \equiv \ln \left(\frac{1}{2} C_d^\circ U_b^* \tau + 1 \right)$. This new variable ξ can be thought of as a measure of how far the

trajectory has progressed, as can be seen by rearranging the solution for X_d^* to state

$$\frac{1}{2}C_d^\circ(X_d^* - X_b^*) = \ln\left(\frac{1}{2}C_d^\circ U_b^* \tau + 1\right). \quad (7.55)$$

As ξ is proportional to a dimensionless distance from breakup and simplifies the equations of motion, it is of fundamental importance to the water jet trajectory problem. Define the time when the droplets impact the ground as τ_{\max} , corresponding to when the maximum range R is obtained. Then

$$X_d^*(\tau_{\max}) = \frac{Rg}{U_0^2} = \eta_R \sqrt{1 + \frac{2}{Fr_{h_0}}} \quad (7.56)$$

using the definitions of X_d^* (equation 7.40) and η_R (equation 7.32). Now equation 7.54 at τ_{\max} can be written

$$Y_d^*(\tau_{\max}) = 0 = -\left(\frac{\frac{1}{2}C_d^\circ U_b^* \tau_{\max} + 1}{C_d^\circ U_b^*}\right)^2 + \frac{2}{C_d^\circ U_b^*} \left(V_b^* + \frac{1}{C_d^\circ U_b^*}\right) \underbrace{\ln\left(\frac{1}{2}C_d^\circ U_b^* \tau_{\max} + 1\right)}_{\text{equation 7.55}} + \frac{1}{(C_d^\circ U_b^*)^2} + Y_b^*. \quad (7.57)$$

After substituting in equation 7.55 at time τ_{\max} and solving this result for $\frac{1}{2}C_d^\circ U_b^* \tau_{\max} + 1$, I obtain

$$\frac{1}{2}C_d^\circ U_b^* \tau_{\max} + 1 = [(C_d^\circ U_b^* V_b^* + 1)C_d^\circ (X_d^*(\tau_{\max}) - X_b^*) + 1 + (C_d^\circ U_b^*)^2 Y_b^*]^{1/2}. \quad (7.58)$$

Substituting this result into equation 7.55 at time τ_{\max} returns an implicit equation for $X_d^*(\tau_{\max})$,

$$C_d^\circ (X_d^*(\tau_{\max}) - X_b^*) = \ln[(C_d^\circ U_b^* V_b^* + 1)C_d^\circ (X_d^*(\tau_{\max}) - X_b^*) + 1 + (C_d^\circ U_b^*)^2 Y_b^*], \quad (7.59)$$

which can be written in terms of η_R using equation 7.56. After writing the above in terms of η_R and substituting in the definitions of X_b^* (equation 7.53), U_b^* (equation 7.51), V_b^* (equation 7.52), and Y_b^* (equation 7.54), I obtain:

$$\begin{aligned}
& C_d^\circ \left(\eta_R \sqrt{1 + \frac{2}{Fr_{h_0}}} - \frac{\langle x_b \rangle / d_0}{Fr_0} \cos \theta_0 \right) \\
&= \ln \left[\left(C_d^\circ \left(\sin \theta_0 - \frac{\langle x_b \rangle / d_0}{Fr_0} \right) \cos \theta_0 + 1 \right) C_d^\circ \left(\eta_R \sqrt{1 + \frac{2}{Fr_{h_0}}} - \frac{\langle x_b \rangle / d_0}{Fr_0} \cos \theta_0 \right) \right. \\
&\quad \left. + 1 + \left(\frac{\langle x_b \rangle / d_0}{Fr_0} \sin \theta_0 - \frac{1}{2} \left(\frac{\langle x_b \rangle / d_0}{Fr_0} \right)^2 + \frac{1}{Fr_{h_0}} \right) \left(C_d^\circ \cos \theta_0 \right)^2 \right]. \quad (7.60)
\end{aligned}$$

Now, for convenience, I define

$$\hat{\eta} \equiv C_d^\circ \left(\eta_R \sqrt{1 + \frac{2}{Fr_{h_0}}} - \frac{\langle x_b \rangle / d_0}{Fr_0} \cos \theta_0 \right) \quad (7.61)$$

$$a \equiv 1 + \left(\frac{\langle x_b \rangle / d_0}{Fr_0} \sin \theta_0 - \frac{1}{2} \left(\frac{\langle x_b \rangle / d_0}{Fr_0} \right)^2 + \frac{1}{Fr_{h_0}} \right) \left(C_d^\circ \cos \theta_0 \right)^2, \quad (7.62)$$

$$b \equiv 1 + C_d^\circ \left(\sin \theta_0 - \frac{\langle x_b \rangle / d_0}{Fr_0} \right) \cos \theta_0, \quad (7.63)$$

so equation 7.60 can be written as

$$\hat{\eta} = \ln(a + b\hat{\eta}). \quad (7.64)$$

In principle equation 7.60 can be solved with an implicit solver. However, I desire an explicit solution to make analysis easier. The range efficiency η_R can be found explicitly in terms of the Lambert W function, which is defined through the equation

$$z = W(z)e^{W(z)}. \quad (7.65)$$

This function is multiple valued as can be seen in figure 7.5. The two real branches are conventionally denoted 0 and -1 .

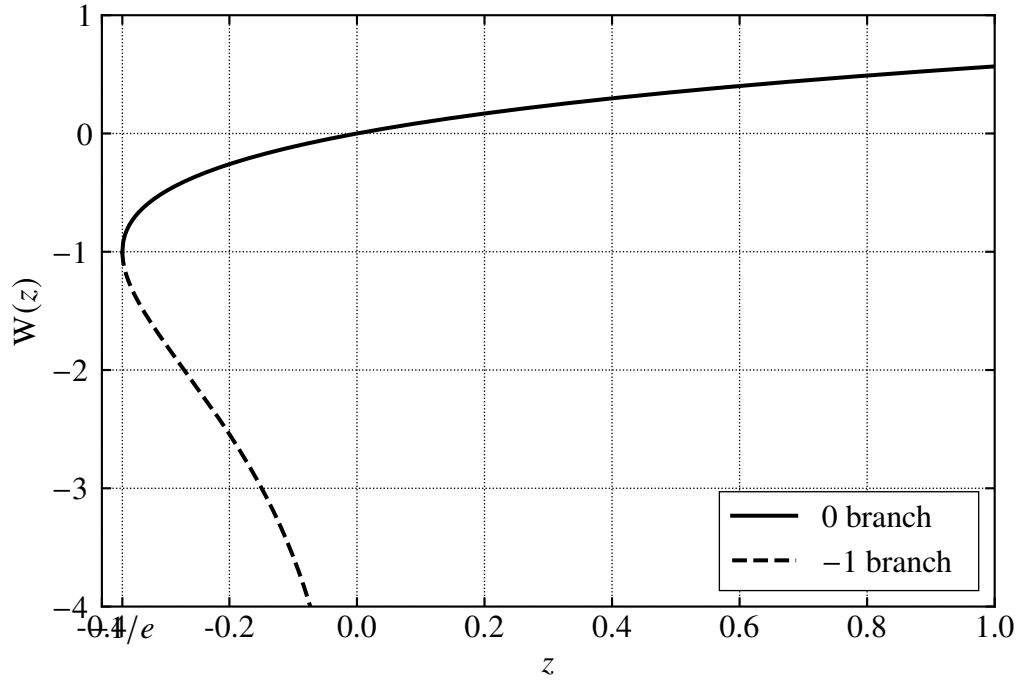


Figure 7.5: The Lambert W function and its two real branches.

One can rearrange equation 7.60 into this form. First, take the exponential of equation 7.64 and factor out b on the right hand side:

$$\exp(\widehat{\eta}) = a + b\widehat{\eta} = b(a/b + \widehat{\eta}). \quad (7.66)$$

Multiply by $\exp(a/b)$:

$$\exp(a/b) \exp(\widehat{\eta}) = b \exp(a/b)(a/b + \widehat{\eta}). \quad (7.67)$$

Take the result to the -1 st power:

$$\exp[-(a/b + \widehat{\eta})] = \frac{b^{-1} \exp(-a/b)}{a/b + \widehat{\eta}}, \quad (7.68)$$

which can be rearranged into a form like the definition of the Lambert W function:

$$-(a/b + \widehat{\eta}) \exp[-(a/b + \widehat{\eta})] = \frac{-\exp(-a/b)}{b}. \quad (7.69)$$

From equation 7.69 and the definition of the Lambert W function (equation 7.65) one can write

$$\mathbb{W} \left[\frac{-\exp(-a/b)}{b} \right] = -\frac{a}{b} - \widehat{\eta} \quad (7.70)$$

or rearranged in terms of $\widehat{\eta}$, the variable which contains η_R :

$$\widehat{\eta} = -\frac{a}{b} - \mathbb{W}_{-1} \left[\frac{-\exp(-a/b)}{b} \right] \quad (7.71)$$

The correct branch is the -1 branch of the Lambert W function, which is specified with the subscript in \mathbb{W}_{-1} . Using the definition of $\widehat{\eta}$ (equation 7.61), the result can be written explicitly in terms of η_R . I repeat all the functional dependencies (C_d^* , a , and b) and conversion to physical range below for convenience.

$$C_d^* \equiv \frac{3}{2} \frac{C_d}{\rho_\ell / \rho_g} \frac{(1 - \alpha)^2}{D_{\max} / d_0}, \quad (7.11)$$

$$a \equiv 1 + (C_d^* \cos \theta_0)^2 \left[\left(\frac{\langle x_b \rangle}{d_0} \sin \theta_0 + \frac{h_0}{d_0} \right) \text{Fr}_0 - \frac{1}{2} \left(\frac{\langle x_b \rangle}{d_0} \right)^2 \right], \quad (7.72)$$

$$b \equiv 1 + C_d^* \cos \theta_0 \left(\text{Fr}_0 \sin \theta_0 - \frac{\langle x_b \rangle}{d_0} \right), \quad (7.73)$$

$$\eta_R = \frac{1}{\text{Fr}_0} \sqrt{\frac{\text{Fr}_{h_0}}{\text{Fr}_{h_0} + 2} \left(\frac{\langle x_b \rangle}{d_0} \cos \theta_0 - \frac{a}{b C_d^*} - \frac{1}{C_d^*} \mathbb{W}_{-1} \left(-\frac{\exp(-a/b)}{b} \right) \right)}, \quad (7.74)$$

$$R = d_0 \left(\frac{\langle x_b \rangle}{d_0} \cos \theta_0 - \frac{a}{b C_d^*} - \frac{1}{C_d^*} \mathbb{W}_{-1} \left(-\frac{\exp(-a/b)}{b} \right) \right). \quad (7.75)$$

where (as before) C_d^* is a reduced drag coefficient, ρ_ℓ is the liquid (water) mass density, ρ_g is the gas (air) mass density, $\text{Fr}_0 \equiv \overline{U}_0^2 / (g d_0)$ is the Froude number, g is gravitational acceleration, D_{\max} is the largest droplet diameter of the spray (assumed constant), and $\text{Fr}_{h_0} \equiv \overline{U}_0^2 / (g h_0)$ is the height Froude number. a and b are model intermediary variables which are used in equation 7.74.

As before for h^* (equation 7.22), R^* (R -star) can be defined, offering a simplifying alternative non-dimensionalization:

$$R^* \equiv \frac{C_d^* R}{d_0} \quad (7.76)$$

so that

$$R^* = \frac{C_d^* \langle x_b \rangle}{d_0} \cos \theta_0 - \frac{a}{b} - W_{-1} \left(-\frac{\exp(-a/b)}{b} \right). \quad (7.77)$$

7.3.3.3 Lambert W function implementations and approximations

The Lambert W function has been implemented in many software packages. In Matlab and Octave, the function `lambertw(-1, z)` computes the value of the -1 branch of the Lambert W function at z . In Python, after importing the `lambertw` function from `scipy.special`, the -1 branch of the Lambert W function can be computed with `lambertw(z, -1)`. The GNU Scientific Library has an implementation⁹. A JavaScript implementation based on the GNU Scientific Library is also available¹⁰.

However, for cases where an implementation is not available (e.g., Excel), an approximation developed in this work could be used:

$$W_{-1}(z) \approx -2 - e^2(z - z_0) - \frac{e^6}{6}(z - z_0)^3, \quad (7.78)$$

where $z_0 = -2e^{-2}$.

The typical series approximations to the Lambert W function are only for the 0 branch, which is not applicable to this case. The 3 term approximation I developed (equation 7.78) is within 1% accuracy for the cases of interest. This approximation is based on a Taylor series centered at the single inflection point of the -1 branch. Approximating the function here is convenient because it reduces the number of terms in the series and the coefficients of the series can be expressed as elementary functions at this location.

⁹https://www.gnu.org/software/gsl/manual/html_node/Lambert-W-Functions.html

¹⁰<https://github.com/protobi/lambertw>

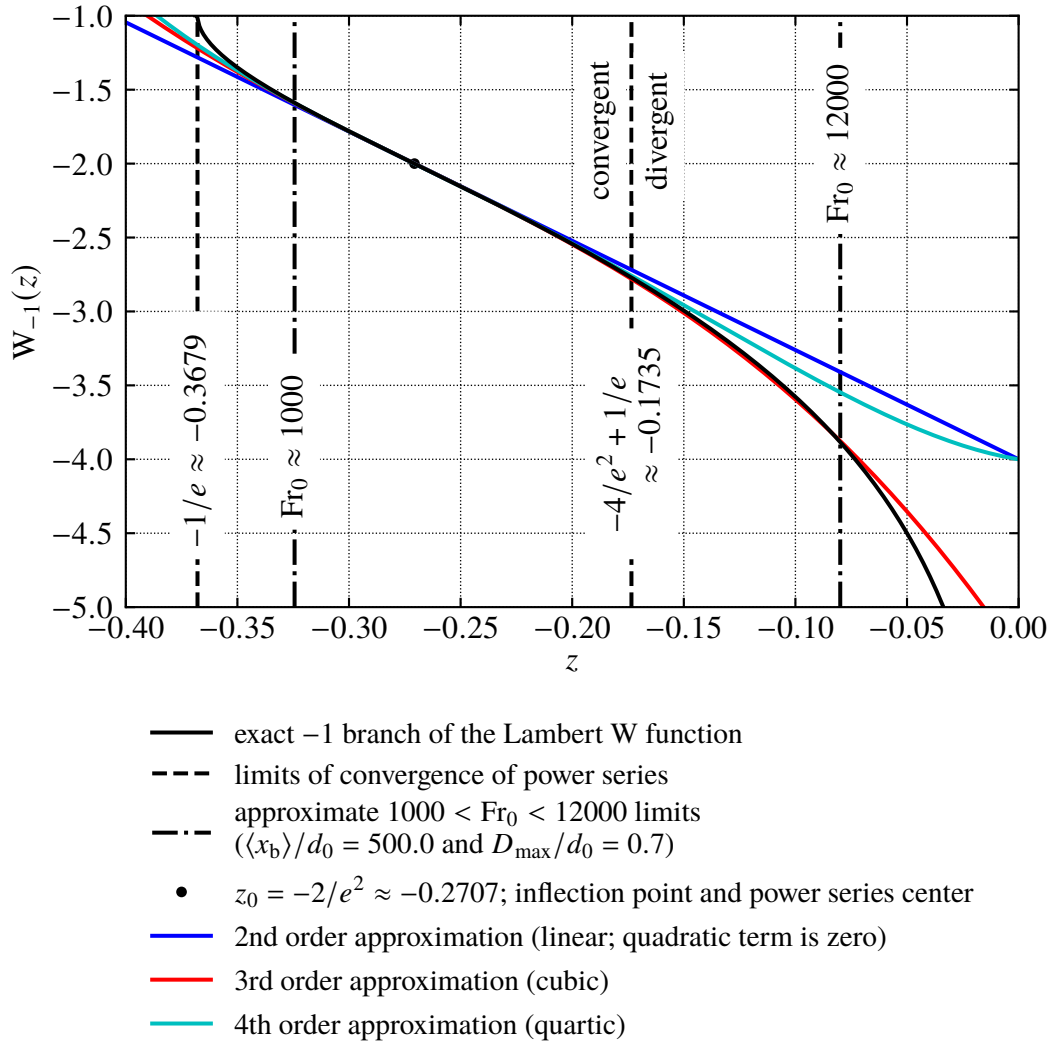


Figure 7.6: The -1 branch of the Lambert W function and Taylor series approximations center at the inflection point.

First, the location of the inflection point must be found. Applying implicit differentiation to the definition of the Lambert W function (equation 7.65) returns

$$\frac{dz}{dz} = \frac{d}{dz} (W_{-1}(z)e^{W_{-1}(z)}), \quad (7.79)$$

$$1 = e^{W_{-1}(z)} W'_{-1}(z) (W_{-1}(z) + 1), \quad (7.80)$$

$$W'_{-1}(z) = \frac{1}{e^{W_{-1}(z)} (W_{-1}(z) + 1)}. \quad (7.81)$$

Taking the derivative of equation 7.80, returns

$$0 = e^{W_{-1}(z)} (W_{-1}(z) + 1) W''_{-1}(z) + e^{W_{-1}(z)} (W_{-1}(z) + 2) (W'_{-1}(z))^2. \quad (7.82)$$

The second derivative can be solved for, leading to

$$W''_{-1}(z) = \frac{-(W_{-1}(z) + 2)}{e^{W_{-1}(z)} (W_{-1}(z) + 1)^2}. \quad (7.83)$$

I'll call the inflection point z_0 . Setting $W''_{-1}(z_0)$ to zero and rearranging returns $W_{-1}(z_0) = -2$, so by using the definition of the Lambert W function (equation 7.65) I find that $z_0 = -2e^{-2}$.

Standard computations of the first, third, and fourth derivatives of the Lambert W function at z_0 return that $W'_{-1}(z_0) = -e^2$, $W'''_{-1}(z_0) = -e^6$, and $W_{-1}^{(4)}(z_0) = 2e^8$. Then the Taylor series approximation to $W_{-1}(z)$ centered at z_0 is

$$W_{-1}(z) = -2 - e^2(z - z_0) - \frac{e^6}{6}(z - z_0)^3 + \frac{e^8}{12}(z - z_0)^4 + \mathcal{O} \left[(z - z_0)^5 \right]. \quad (7.84)$$

The -1 branch starts at the branch point, $z = -1/e \approx -0.3679$, where the slope is vertical and the Lambert W function switches from the -1 branch to the 0 branch. Unfortunately, the radius of convergence of the full power series is bounded by the location of the nearest singularity, which is at the branch point, $z = -1/e$. So the power series is divergent for $z > -4/e^2 + 1/e \approx -0.1735$, which is within the range of the argument z expected. See figure 7.6 for an illustration of the Lambert W function, the series

approximations to the Lambert W function, the expected span of the argument of the Lambert W function, and the region of convergence of the series approximations. The quartic approximation barely performs any better than the linear approximation for this reason. But, purely by coincidence, the third order approximation follows the exact curve closely up to $z \approx -0.07$, beyond the upper limit of where the series converges. This means that the third order approximation is within 1% up to an approximate Froude number of 12000.

Consequently, the following approximation is recommended:

$$W_{-1}(z) \approx -2 - e^2(z - z_0) - \frac{e^6}{6}(z - z_0)^3, \quad (7.78)$$

where again, $z_0 = -2e^{-2}$.

7.3.3.4 Model validation and analysis

Model validation. The analytical model was compared against experimental data from Theobald [The81], the only source for which breakup length ($\langle x_b \rangle$) measurements were available for all data points, or could be reasonably estimated. Theobald also has the only measurements of water jet trajectories made indoors, eliminating the effect of wind. Some additional lower angle data (without known breakup length) comes from the outdoor experiments of Hickey [Hic73] — the breakup length in this case was estimated from equation 3.28 with the turbulence intensity assumed to be 10%.

Note that there is appreciable uncertainty in most of this data. Even using data without the influence of wind, this uncertainty is appreciable. Experiments not completed in time for this dissertation suggest that pressure variations between shots are the largest contributor to the uncertainties. Higher precision pressure regulation is necessary for proper scientific study of water jet trajectories. With these limitations in mind, the model can still be evaluated, but will require comparison against better data in the future.

Theobald's provided breakup length curves did not cover the highest Weber numbers. When the Weber numbers were too high, the highest value of the breakup length available

was chosen. The breakup length measurements are shown in figure 7.7 as a function of Weber number ($We_{\ell 0} \equiv \rho_{\ell} \bar{U}_0^2 d_0 / \sigma$). Also included is an approximate laminar trend (for $Re_{\ell 0} \gg We_{\ell 0}$, where $Re_{\ell 0} \equiv \bar{U}_0 d_0 / \nu_{\ell}$) and an empirical regression for the turbulent surface breakup regime from § 3.4.10. Theobald was British and his nozzles were smaller than typical US nozzles, leading to smaller Weber and Reynolds numbers and a regime change (downstream transition regime) compared against US water jets. From the perspective of the trajectory model, this is acceptable as long as the breakup length is known, but it means that the empirical regression for $\langle x_b \rangle$ (equation 3.28) is not applicable for Theobald's data.

The maximum droplet diameter, D_{\max} , was the only variable available for calibration. These large droplets are unstable and will break up on their own. The analytical model does not have a droplet breakup model, and consequently the maximum droplet diameter is an *effective* maximum droplet diameter in the analytical model. This is expected to be smaller than the actual maximum, but on the same order of magnitude. I chose $D_{\max} / d_0 = 0.8$ as this best fit the available data. This is consistent with the available experimental data for the maximum droplet diameter.

See figure 7.8 for the comparisons of range efficiency as calculated by the analytical model and experimentally measured. The model is not perfect, but it reasonably collapses the data for the three different nozzles tested. Note that this model is still reasonably accurate despite the fact that Theobald has many cases with firing angles larger than those acceptable in the flat fire approximation.

Sensitivity analysis. While severe jet breakup is well accepted to be detrimental to the performance of water jet trajectory systems, figure 7.9 makes it clear that the majority of the problems of jet breakup would come from reduced droplet size rather than reduced breakup length. While doubling the breakup length and disabling air entrainment entirely ($\alpha = 0$) lead to only modest changes in jet efficiency, reducing the maximum droplet diameter from $3d_0$ to d_0 massively reduces jet efficiency. Also visible in this plot that the jet efficiency decreases appreciably as the Froude number increases.

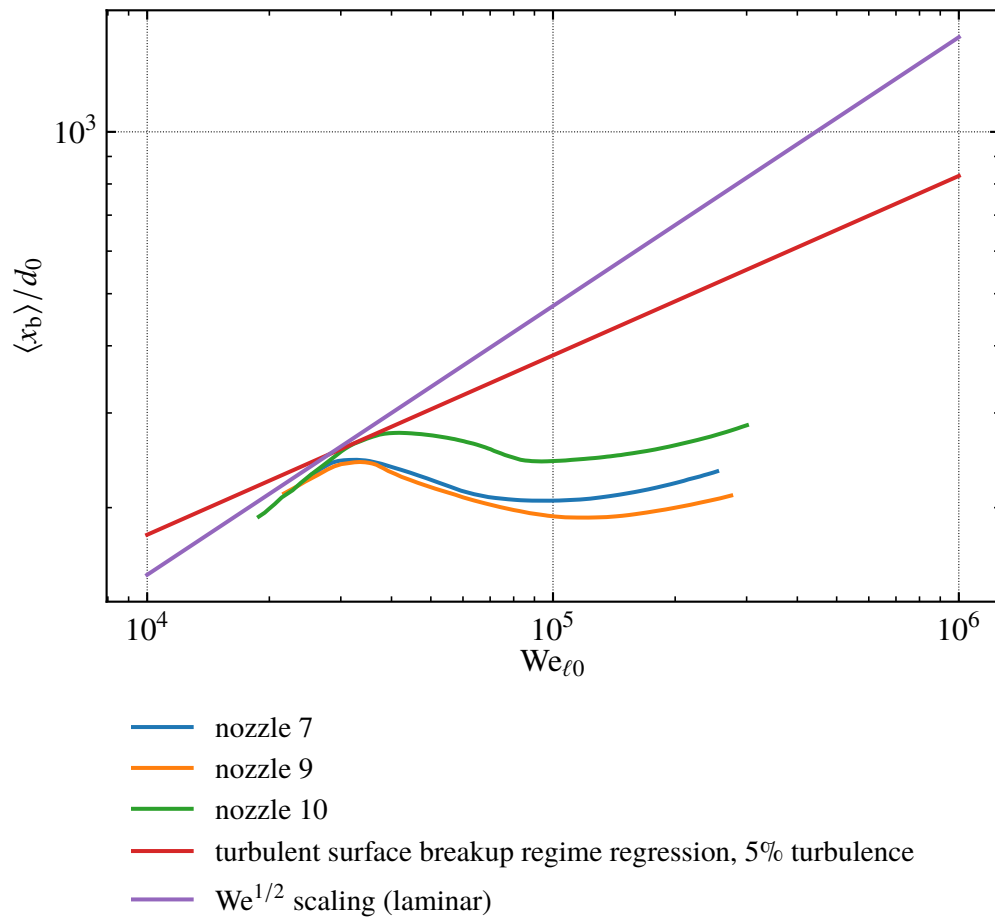


Figure 7.7: Breakup length curves from Theobald [The81] for three different nozzles along with a regression for the turbulent surface breakup regime (equation 3.28) and the expected laminar trends.

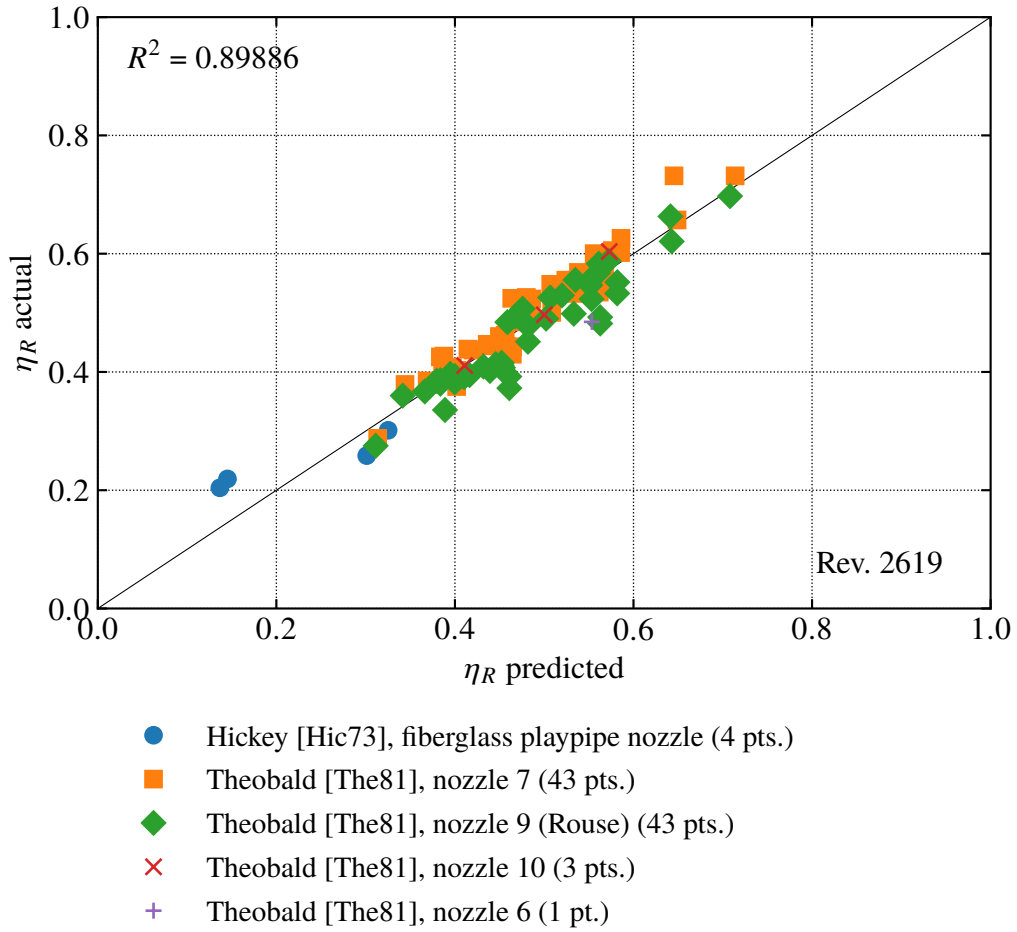


Figure 7.8: Comparison of R predictions (equation 7.74) to experimental measurements.

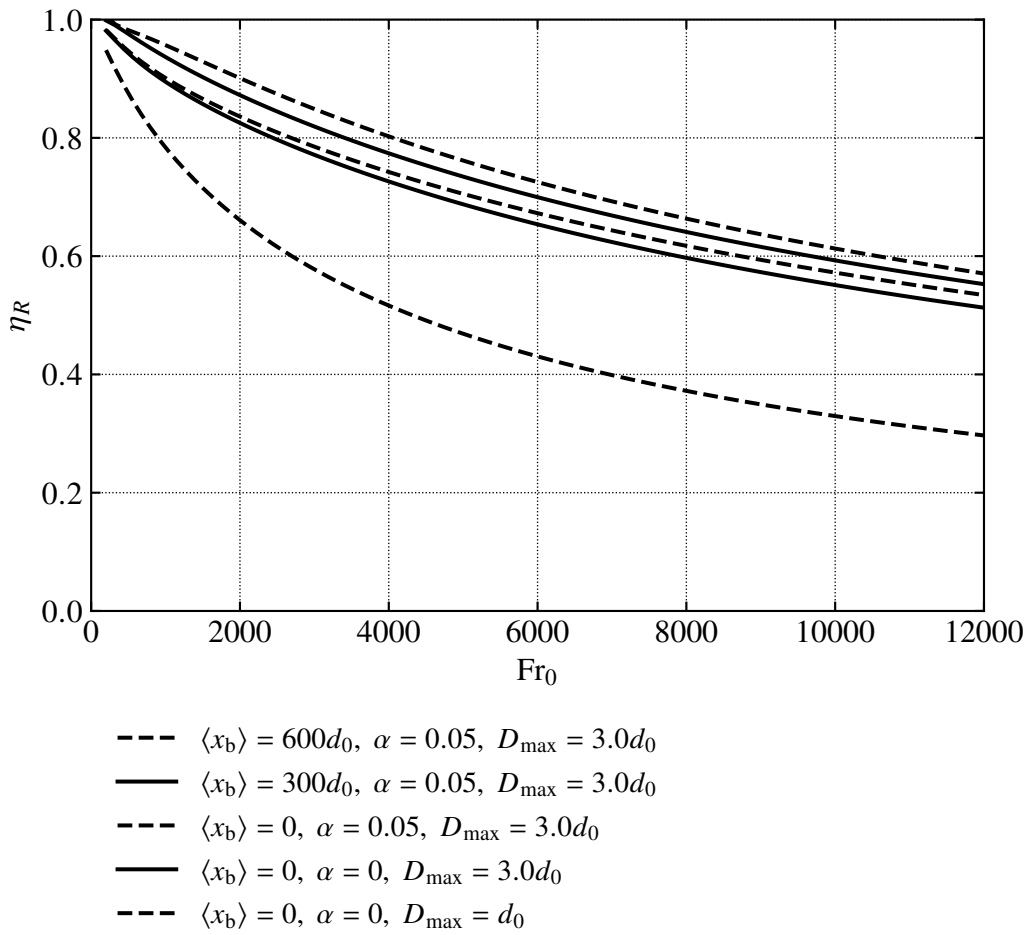


Figure 7.9: General trends of range efficiency η_R as a function of Fr_0 for various examples. The lines are ordered as written in the legend, i.e., the lowest line in the legend is the lowest line in the plot

Why the flat fire approximation is accurate at larger angles than one might expect.

The flat-fire approximation is known to be reasonably accurate up through angles as large as 45° , as shown by Warburton, Wang, and Burgdörfer [WWB10, p. 99].

A small contribution to this comes from the breakup process. The initial firing angle the flat-fired equations see is not θ_0 . Instead the appropriate angle is the angle the jet makes when breakup occurs, θ_b . The tangent of this angle is

$$\tan \theta_b = \tan \theta_0 - \frac{\langle x_b \rangle / d_0}{Fr_0 \cos \theta_0}. \quad (7.85)$$

Thus, θ_b is always smaller than θ_0 . However, it is not much smaller; the deviation is on the order of a single degree in a typical case. Thus, this effect does not entirely explain the success of the flat-fired approximation.

7.4 Conclusions

Typical models of water jet trajectories treat the jet as a collection of non-interacting droplets exiting the nozzle. This implicitly assumes that the breakup length of the jet is zero. However, conventional fire hose nozzle design guidelines emphasize reducing breakup (increasing the breakup length) as a way to improve the range of water jets. This effect can not be reproduced in typical models. Models also frequently neglect air entrainment effects. To address these shortcomings, a new analytical model of the trajectory of a water jet was developed using a small angle approximation called the flat fire approximation. This model considers both the breakup length and air entrainment. The model was validated against existing data from the literature, most of which was conducted indoors (improving the reliability of the experiments) and most of which had measured breakup lengths (in contrast to typical experiments).